HITUBES PROJECT

DESIGN AND INTEGRITY ASSESSMENT OF HIGH STRENGTH TUBULAR STRUCTURES FOR EXTREME LOADING CONDITIONS

Deliverables 5.1, 5.2 & 5.3

D5.1: Refined material parameter formula depending upon fast loading.

D5.2: Simulation data on welded joints relevant to the structures under study.

D5.3: Simulation data on bolted joints relevant to the structures under study.

Authors

Jean-Pierre Jaspart, Jean-François Demonceau, Long Van Hoang, Ly Dong Phuong Lam
Spyros Karamanos , Philip Perdikaris, Aglaia Pournara, Charis Papatheocharis, George Varelis

Contributing Partners

Université de Liège, Belgium
University of Thessaly, Greece

Table of Contents

D5.1: Refined material parameter formula depending upon fast loading- Deliverable D5.1

It is recognized on one hand, that the rate of loading has an effect on the material properties. In this respect, see References at the end of this section. On the other hand, flexible structures like slender foot- and cycle-bridges can be very sensitive to extreme winds owing to typhoons [1] or anthropic actions, e.g. human beings walking. Similar effects can happen in the case of high-speed trains [2].

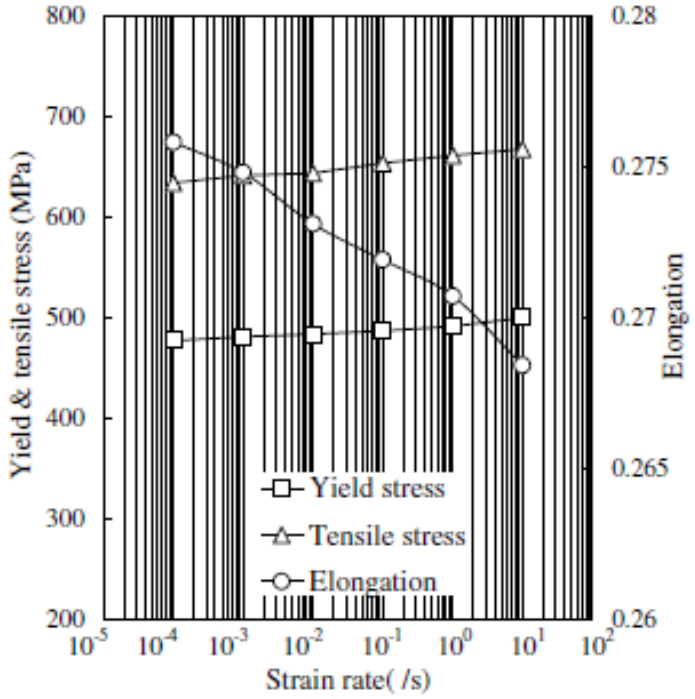

Figure 5.1.1: Distribution of mechanical properties for strain rate

Even though strain-rate effects influence the yield stress, the tensile stress and the elongation of the material, see Fig. 5.1.1, after Chang Kyong-Ho et al. [3], these affects are usually not taken into account, unless impact or blast are considered [4]. These effects are not known for HSS. As a result in order to investigate such phenomena, tests under low-cycle fatigue loading were performed up to 1/s strain rate by ITMA as shown in the deliverable D4.1.

In order to reproduce these effects, some formula was reviewed and reported here. Previous works by Rao reported in Lamarche [5] indicated that the dynamic yield stress, σ_{yd}, can be expressed as a function of the strain rate as follows:

$$\frac{\sigma_{yd}}{\sigma_{ys}} = 1 + c\left(\dot{\varepsilon}\right)^{n} \qquad (1)$$

where σ_{ys} is the yield stress under static loading, and C, n are constants to be determined experimentally.

For a regular -strength steel A36 -equivalent to S235-, the following formula was proposed:

$$\frac{\sigma_{yd}}{\sigma_{ys}} = 1 + 0.021\dot{\varepsilon}^{0.26} \qquad (2)$$

Alternatively, the following formula can be used:

$$\sigma_{yd} - \sigma_{ys} = 3.2 + 0.001\dot{\varepsilon} \quad \text{for } 200 < \dot{\varepsilon} < 1000 \qquad (3)$$

Based on the tests performed by ITMA, Figure 5.1.2 was drawn for TS590 for four values of strain rates, i.e. 0.001, 0.01, 0.1 and 1/s. Maximum value of strain rate, i.e. 0.1/s derived from the analysis of 'Ponte del Mare' footbridge subject to wind and carried out in Task 2.4.

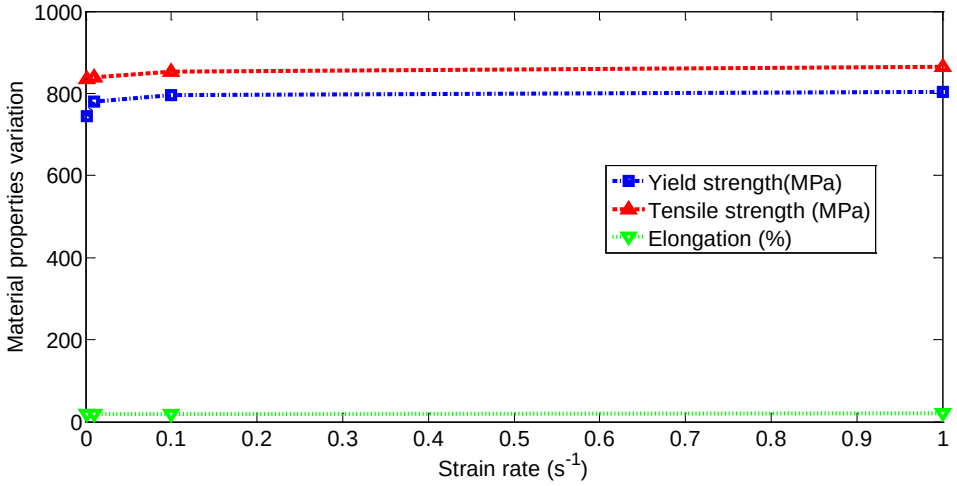

Figure 5.1.2: Distribution of mechanical properties of TS590 for four strain rates

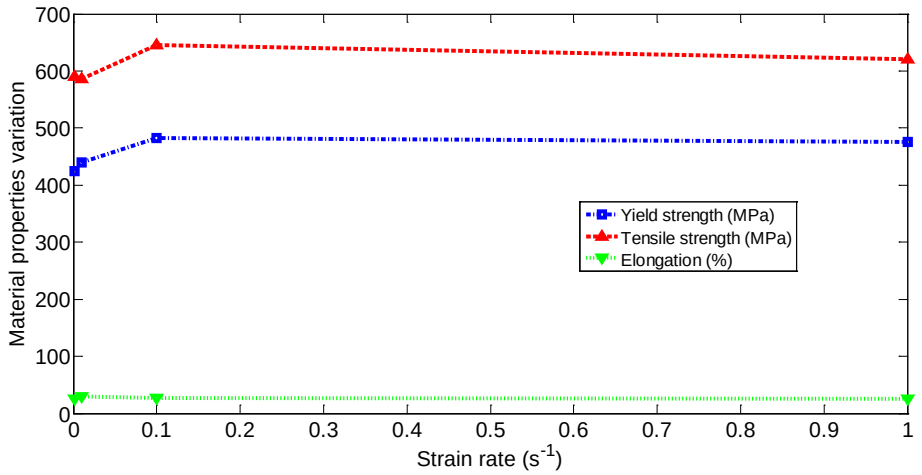

Figure 5.1.3: Distribution of mechanical properties of S355 for four strain rates

Figures 5.1.4 and 5.1.5 are plotted on the logarithmic strain rate values. One can notice that Figure 5.1.4 shows an increasing YS and TS similar to the one in Figure 5.1.1.

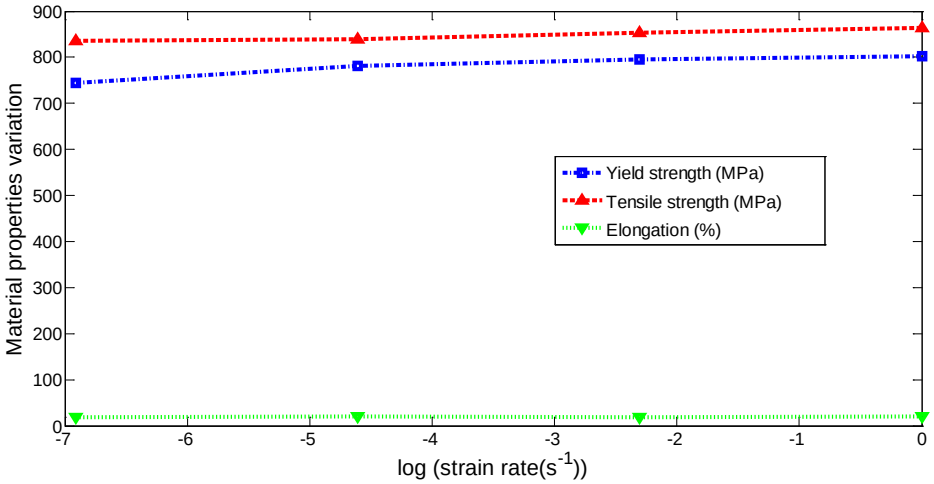

Figure 5.1.4: Distribution of mechanical properties of TS590 for four (log) strain rates

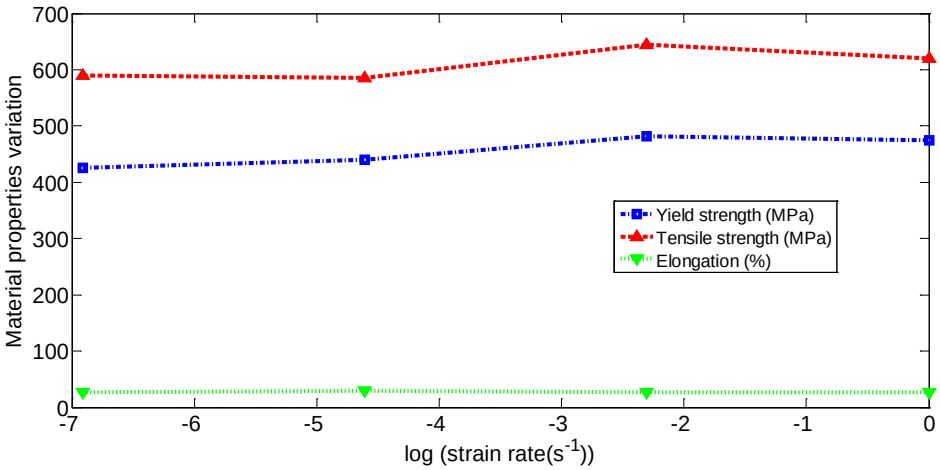

Figure 5.1.5: Distribution of mechanical properties of S355 for four (log) strain rates

Eq. (1) was fitted with the test data for both the TS590 and S355 and the coefficients c and n were evaluated. The values are given below in Table 5.1.1.

Table 5.1.1 Coefficients of the material parameter formula for TS590 and S355

	σ_{ys} (MPa)	c	n
TS590	745	0.085	0.19
S355	425	0.137	0.22

Table 5.1.1 shows that the TS590 steel examined exhibits lower value of c and n than S355 steel. As a result, the high strength steel examined appears to be less sensitive than regular structural steel.

References

[1] Li Z.X, Chan T.H.T and Ko J.M. (2002), "Evaluation of typhoon induced fatigue damage for Tsing Ma Bridge", Engineering Structures 24, 1035–1047.

[2] Castellani, Alberto (2000), "Vibrations Generated by Rail Vehicles: A Mathematical Model in the Frequency Domain", Vehicle System Dynamics, 34: 3, 153 — 173.

[3] Chang Kyong-Ho et al. (2009), "Strain-rate dependence of mechanical behavior and hysteretic characteristics of TMCP steel (SM570-TMC) and its modeling", Computational Materials Science 45, 669–673.

[4] Xiuhua Z, et al. (2008), "Numerical Simulation of Dynamic Response and Collapse for Steel Frame Structures Subjected to Blast Load" Transaction of Tianjin University 14, 523-529.

[5] Charles-Philippe Lamarche (2009), "Development of Real-time dynamic substructuring procedures for the seismic testing of steel structures", PhD thesis – Ecole Polithecnique de Montreal.

D.5.2. Determination of S-N data for welded and bolted relevant to connections and refinement of the component method

In the framework of the WP 5, the simulation of the tests on the examined tubular joints has been conducted. A detailed numerical model has been developed for the simulation of the tests on the X-joints. The numerical model represents the actual dimensions of each welded joint. The weld geometry has been modeled in detail, according to the provisions of the American Structural Welding Code AWS D1.1 (AWS, 2004).

The model is developed in ABAQUS and uses 8-node, quadratic, reduced integration solid elements (C3D8R) for most of the chord, whereas 4-noded solid elements (C3D4) are used in the brace part and the weld region of the joint on the chord (Varelis et. al., 2012). Moreover, the mesh size is denser near the weld region in order to provide accuracy in the simulation results and time-effective simulations. Only half of the joint is modeled, taking advantage of symmetry and applying the appropriate symmetry conditions. The model is shown in Fig. 2.1. The same numerical model has been used for all the simulations of the various types of tests by properly modifying the applied boundary conditions in order to match those conditions applied by the test set-up to the specimen at each case.

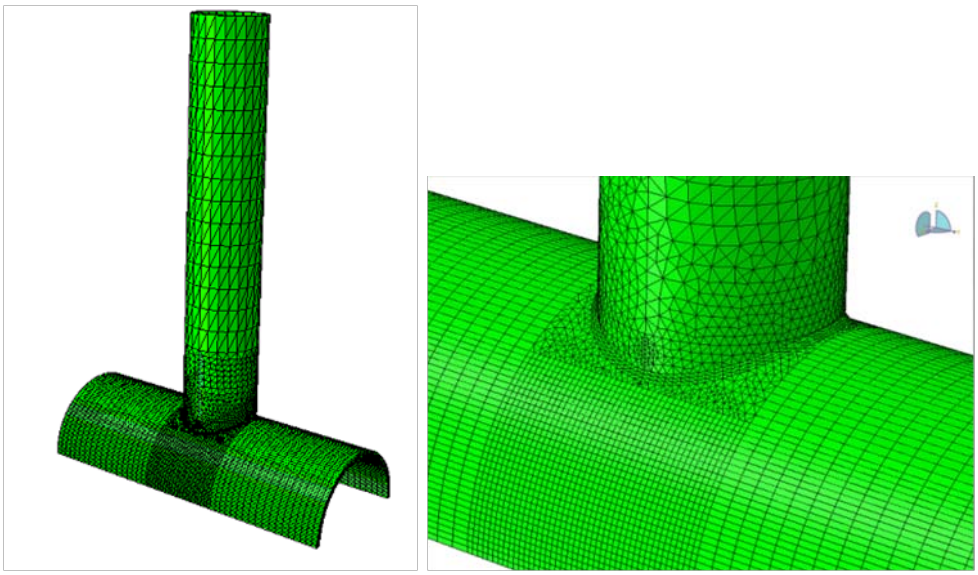

(a) (b)

Figure 2.1: Numerical model developed: (a) General view (b) Weld region.

The numerical results have been obtained using a material model of J_2 flow plasticity, accounting for large strains. For the purposes of the present analysis, linear kinematic hardening has been employed. A bilinear stress-strain curve which compares fairly well with the uniaxial tensile test data was used for the simulations (Fig.2.2).

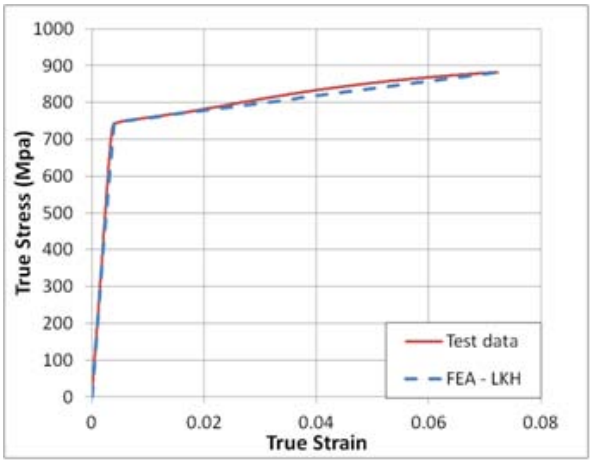

Figure 2.2: Uniaxial steel material stress-strain curve.

D.5.2.1. Numerical results for joints under out-of-plane bending

For the simulation of the OPB tests, the joint geometry was modeled according to the measured dimensions of the tubular members, which are very close to the nominal ones, considering a uniform thickness of the chord and the brace. As displayed in Fig. 2.3, the experimental measurements can be numerically reproduced quite accurately for monotonic and cyclic loading conditions.

It is worth noticing that the overall joint behavior is sensitive to rather small variations of the chord thickness value. This difference is attributed to the earlier initiation of inelastic behavior when the chord thickness becomes smaller, so that the joint resistance is significantly reduced. In all cases of applied loading type, the results show that the numerical model is capable of simulating accurately the experimental procedure and representing the experimental results.

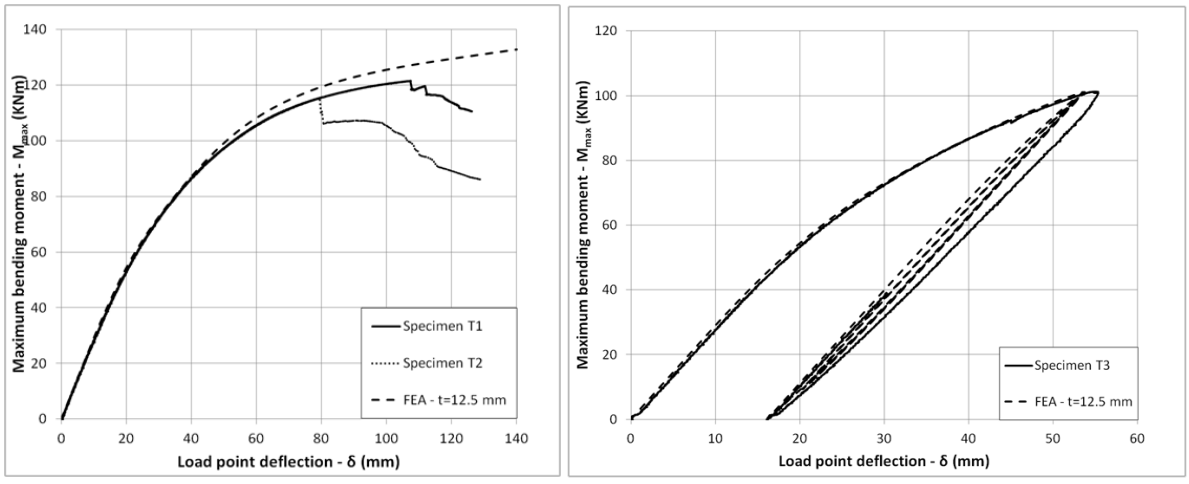

(a) (b)

Figure 2.3: Out-of-plane bending tests - comparison of the numerical and experimental load vs. displacement curves: (a) Monotonic, (b) Cyclic loading.

The strain concentration factor (SNCF) and the stress concentration factor (SCF) has been also evaluated numerically. The numerical SNCF value is estimated equal to 7.18, higher than the experimentally evaluated value. According to CIDECT guidelines (2001), the corresponding SCF for the joint under consideration is equal to 9.82, whereas the numerical model results to a SCF value equal to 6.16 using a linear extrapolation and 8.19 using quadratic extrapolation, as shown in Fig. 2.4(b). The above differences are attributed to the sensitivity of the strain/stress field near the weld toe in terms of local conditions (notch effect).

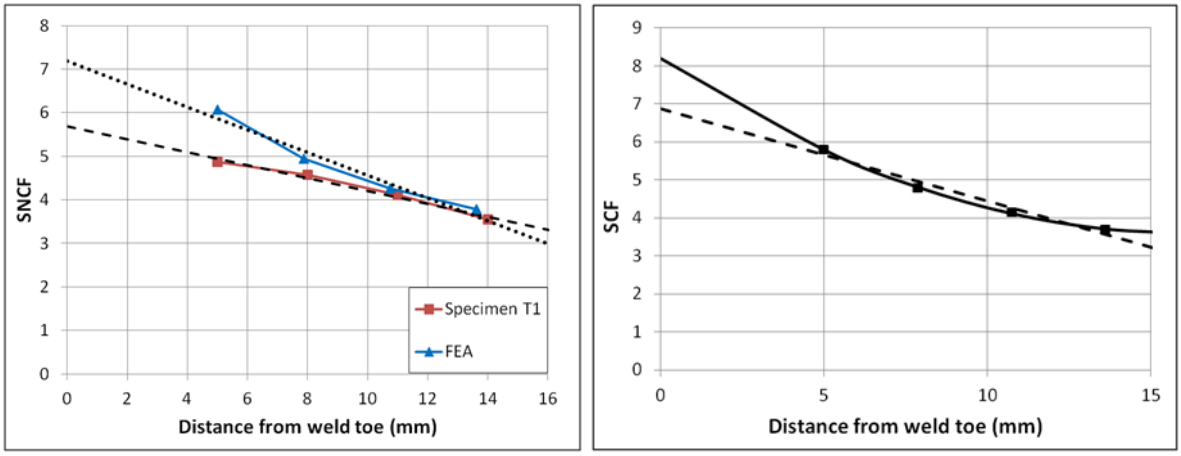

(a) (b)

Figure 2.4: (a) SNCF and (b) SCF evaluation for out-of-plane bending moments.

Towards better understanding of the chord deformation at the weld area, the deformed chord geometry is shown in Fig. 2.5, corresponding to a joint section at the chord middle plane. The concentration of plastic deformation near the weld-toe area is significantly higher than the one located at the weld of the joint, so that the location of cracking initiation at the weld-toe is verified. The deformation mode presented in Fig. 2.5(a) has been also observed in the experiments and indicates that there is a significant change of chord curvature near the weld toe region, which reaches a critical value at a distance of about 5 times the chord thickness.

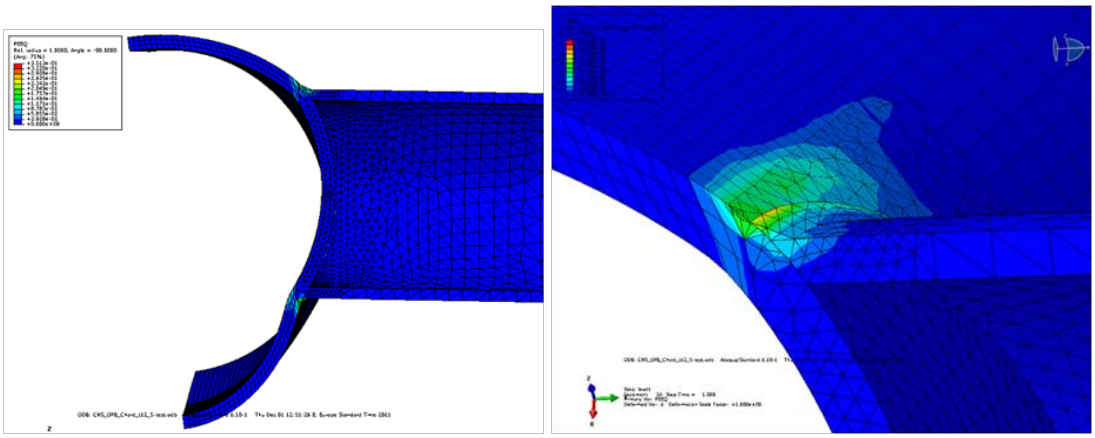

(a) (b)

Figure 2.5: Out-of-plane bending test simulation. Mid-span section (a) Deformed chord geometry (b) Equivalent plastic strain distribution at the weld-toe area

D.5.2.2. Numerical results for joints under in-plane bending

The same model has been used for the simulation of the IPB tests (monotonic and cyclic). The predictions of the model are in good agreement with the experimental measurements for both types of loading, as presented in Fig. 2.6. The stress concentration factor has been evaluated according to the provisions of CIDECT No. 8 (2001) and it is found equal to 3.48. It is observed that the distribution of plastic deformations under this kind of loading is widely spread along the circumference of the weld (Fig. 2.7), which justifies the shear-dominant type of failure observed in the experiments. According the provisions of EN 1993-1-8 (2002) and by adopting the actual characteristics of the joint, the joint resistance under IPB is equal to 202 KNm and the failure mode is punching shear, as justified by the numerical results as well. The predicted value is significantly lower than the experimentally measured resistance (32.6% and 24.5% for weld conditions A and B respectively), but lays on the safe side.

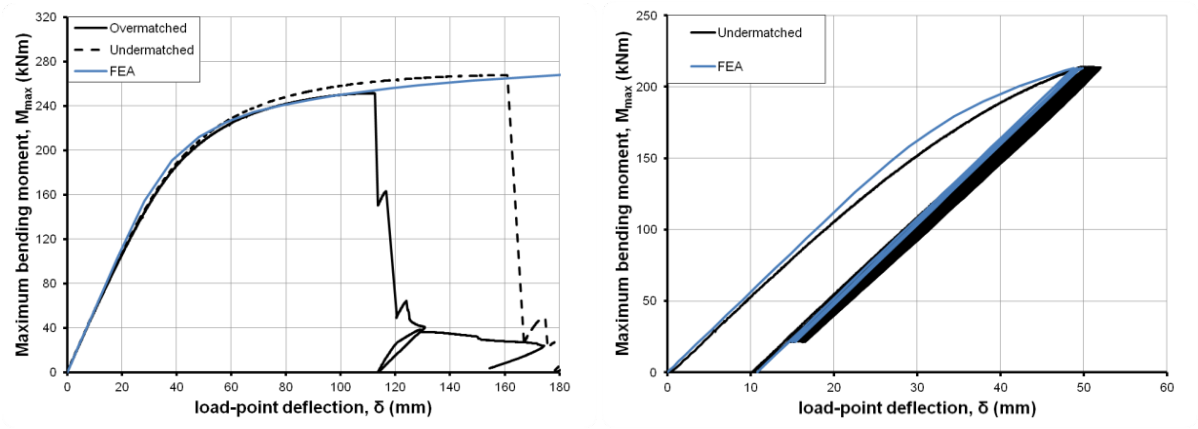

(a) (b)

Figure 2.6: In-plane bending test and numerical simulation results: (a) Monotonic loading, (b) Cyclic loading.

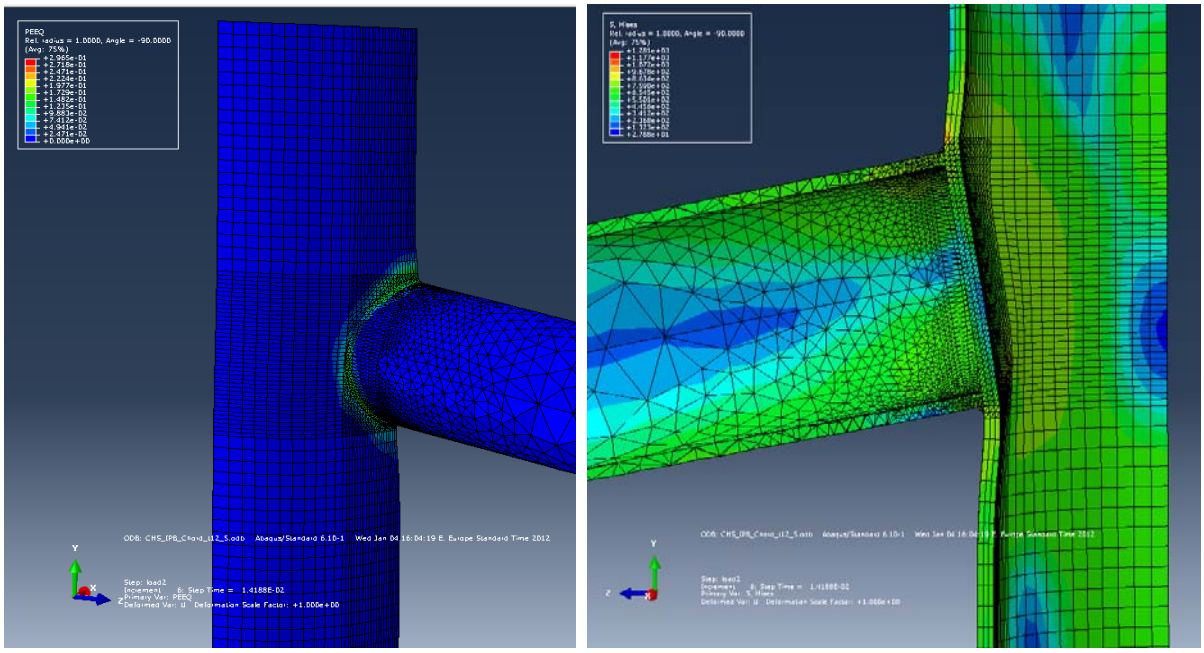

Figure 2.7: In-plane bending test simulation. (a) Equivalent plastic strain distribution at the weld-toe area, (b) Deformed chord geometry - mid-span section

D.5.2.3. Simulation of axial loading tests

The predictions of the numerical model for axial loading of the joint are presented in Fig. 2.8(a). The most important observation is that the joint exhibits different behavior when subjected to axial compression or axial tension loads, as shown in the load-displacement curves. The deformed geometry of the joint under compressive loading is presented in Fig. 2.8(b).

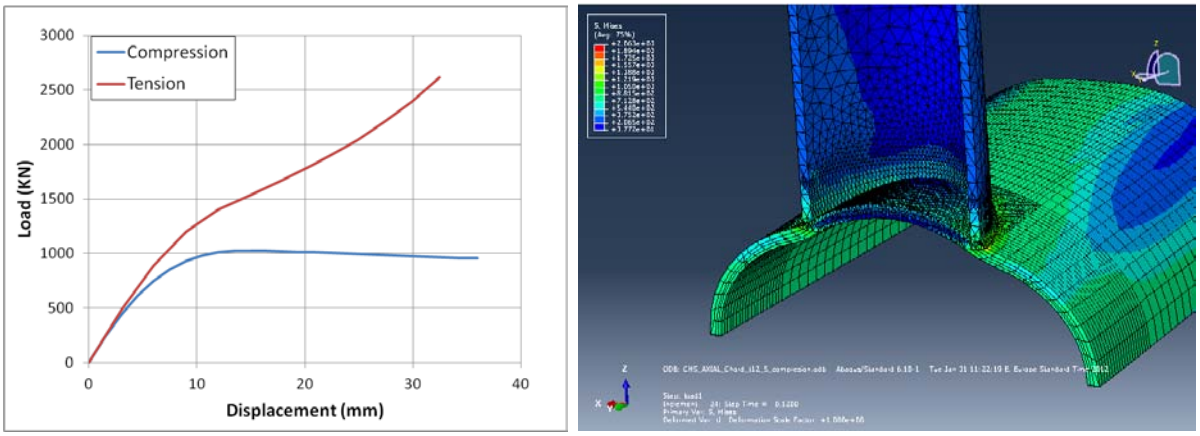

Figure 2.8: Numerical simulation of the X-joint subjected to axial compression and tension loading (a) Load-displacement curves and (b) deflected shape under axial compression.

The axial cyclic loading test has been simulated using the aforementioned numerical model. The simulation results are in good agreement with the experimental measurements. The predicted load displacement curve is compared with the experimental curve in Fig. 2.9(a). In addition, the location of the crack has been also verified by the numerical model, which predicts a high concentration of plastic deformations at the weld toe area of the chord saddle, as shown in Fig. 2.9(b).

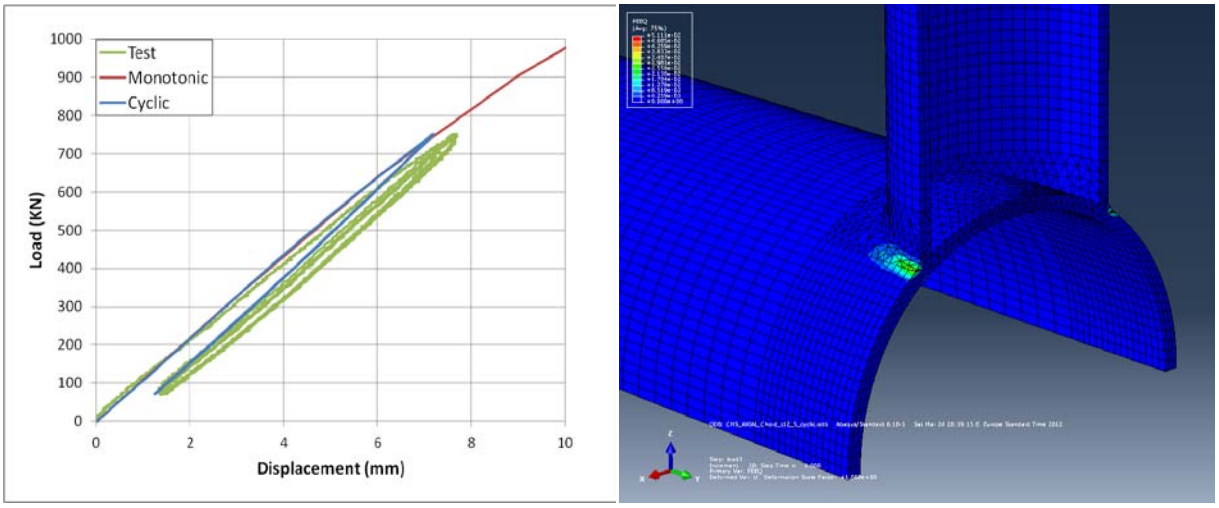

Figure 2.9: Numerical simulation of the X-joint subjected to cyclic axial loading (a) Load-displacement curves and (b) concentration of plastic deformations.

D.5.2.4. References

[1] EN 1993-1-8. (2002). Eurocode 3: Design of steel structures – Part 1-8: Design of joints, European Committee for Standardization.

[2] AWS D1.1/D1.1M: (2004), Structural Welding Code – Steel.

[3] CIDECT No. 1. (1991). Design Guide for Circular hollow Sections (CHS) under Predominantly Static Loading

[4] CIDECT No. 8. (2001). Design Guide for Circular and Rectangular Hollow Section Welded Joints under Fatigue Loading

[5] Varelis, G. E., et al. (2012). Structural performance of TS590 high-strength steel welded tubular joints under extreme bending loading. ISTS 14, London, United Kingdom.

[6] Agreskov H. (1976) High strength bolted connections subject to prying. J. Struc Div.

[7] Dong P. A (2001) structural stress definition and numerical implementation for fatigue analysis of weld joints. International Journal of Fatigue 23 865-876.

D5.3: Simulation data on bolted joints relevant to the structures under study- Deliverable D5.3

The main objective of the numerical simulation campaign was to simulate the behaviour of the joints under monotonic and cyclic loading and simulation of the hot-spot stress at the "hot" zones (at the change of geometry) in the joints. The tests on the bolted joints were reported in Deliverable D4.4 [1].

Numerical simulations were performed with the finite element program LAGAMINE developed by the department ArGEnCo of the University of Liege, Belgium [2].

D.5.3.1 FE model

The FE model is shown in Figure.5.3.1. The tube, the plate and the bolts are modelled by BLZ3D element while the contact surfaces are modelled by CFI3D element [2]. The shank length (Agerskov's length [3]) is adopted for the bolt (Fig.5.3.2 and Table 5.3.1). The thread area is used for the bolt shank.

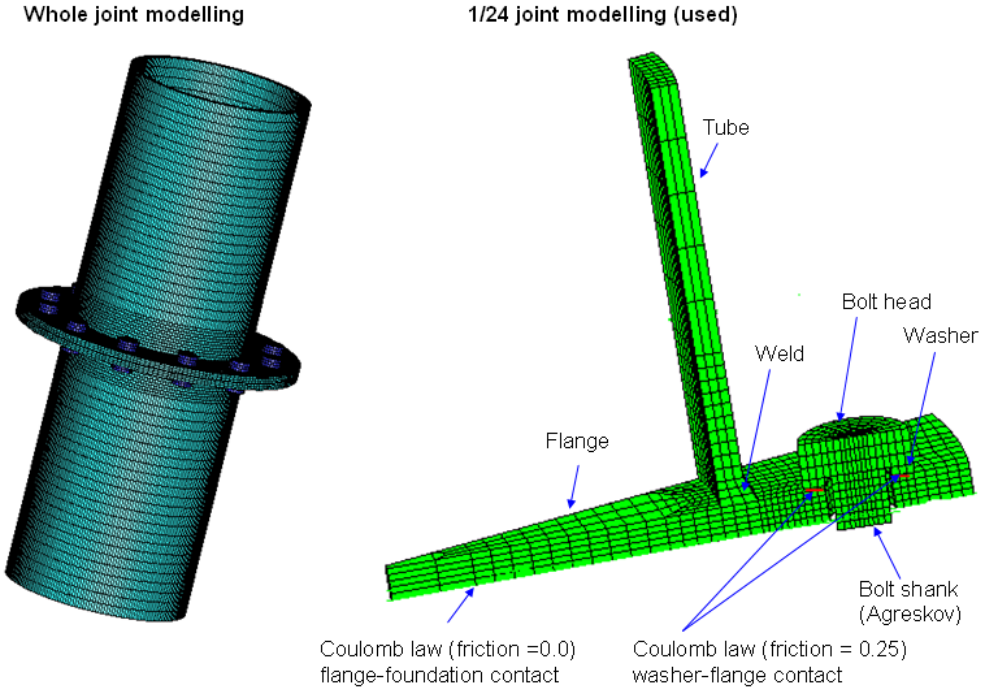

Fig. 5.3.1 FE model

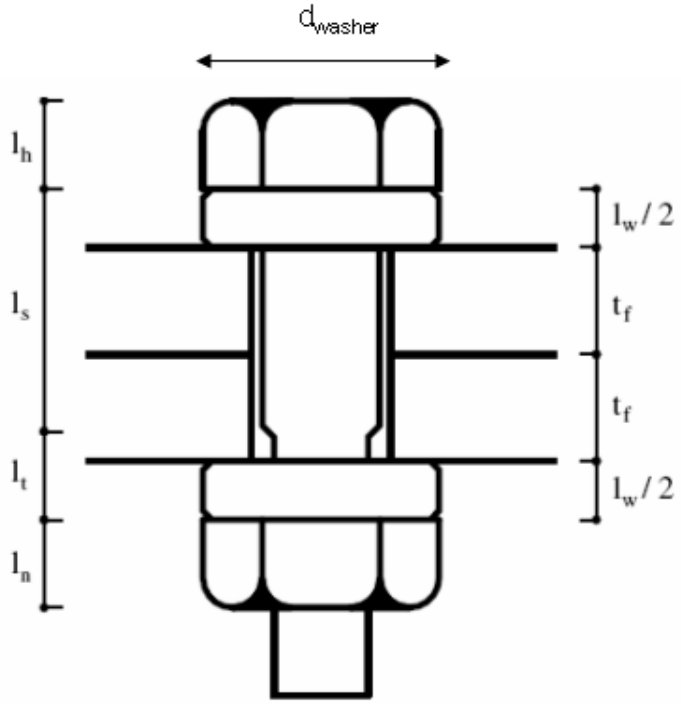

Fig.5.3.2. Bolt geometry in Agreskov's model

Table 5.3.1: Detail value of bolt geometries (Fig.A5.2)

Bolts	A_b (mm^2)	A_s (mm^2)	t_f (mm)	h_h (mm)	l_n (mm)	l_s (mm)	l_t (mm)	l_w (mm)	d_w (mm)	l_{eff} (mm)
M27 (con.1)	573	459	15	17	21	30	8	8	50	510
M20 (con.2)	314	245	20	12,5	15	30	16	6	37	540

D.5.3.2 Modelling of the initial deformation of the flanges

Due to the heat-effect of the weld operation, the flanges deform as the show of Fig.5.3.3. In the joints using the preload bolts, the initial deformation of the flanges influent the initial stiffness and the distribution of stress in the joint components (the tube and the flanges) leading to the change of the HCF strength of the joints. Therefore, the modelling of the initial deformation of the flanges is very important for the case of determination of stress range to calculate the HCF strength.

By the simplification of the meshing procedure, in our modelling the flanges remain plan while the rigid foundation has the form as the show on Fig.5.3.3. From the measurement of Δ (see [1]), two value of 2,75 mm and 1,82 mm are used for the configuration 1 and the configuration 2 respectively.

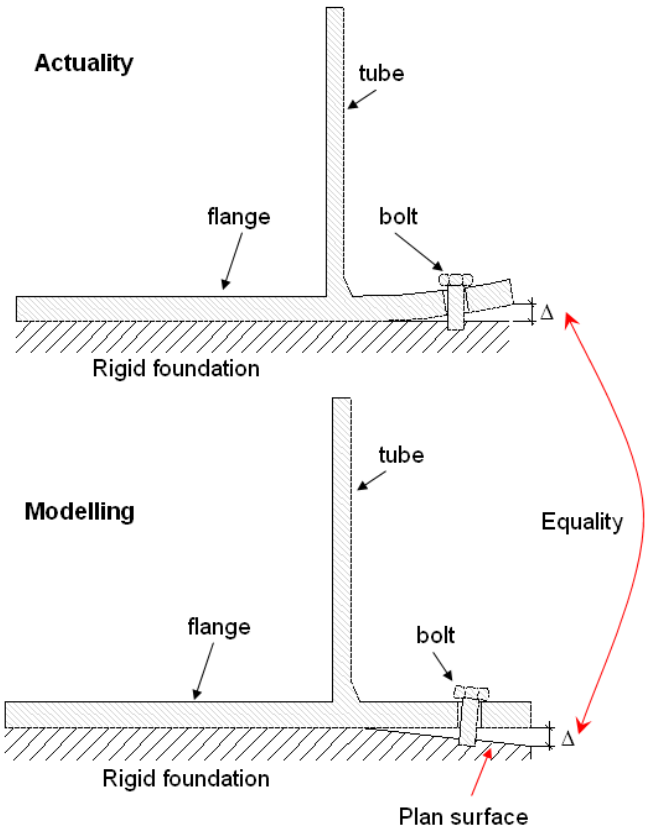

Fig.5.3.3 The modelling of the initial out-of-plan of the flanges

D.5.3.3 Material characteristics

From the nominal σ-ε curve given by the coupon tests (see D4.4 [1]), the natural σ-ε curves for the material are established. By the simplification reason, the multi-linear curve is adopted for the natural σ-ε relation (Figs. 5.3.4 and 5.3.5).

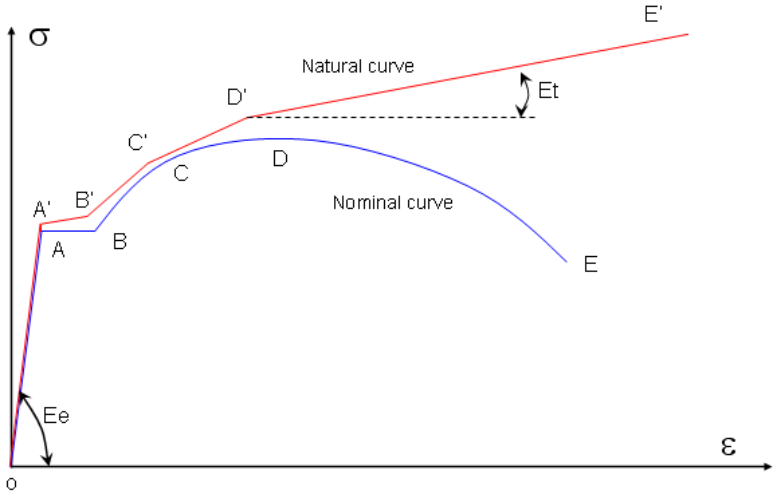

Fig.5.3.4. σ - ε curve of the flange material (mild steel)

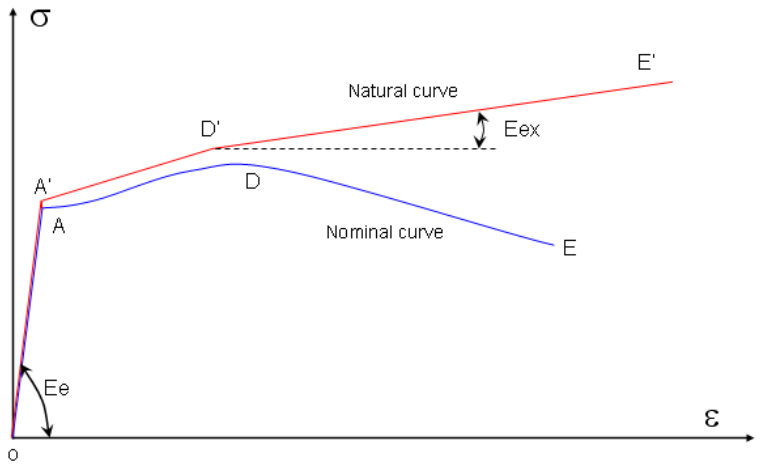

Fig.5.3.5. σ - ε curve of the tube and the bolts material (high strength steel)

The key values to have the natural curve are determined as the following.

By using the results of the coupon tests, some values are chosen and fixed with no much error: ε_B, ε_C, ε_D, E_e, $\sigma_A = \sigma_B$, σ_C, σ_D (Table 5.3.2). As the description in D4.4 [1], the test on bolts don't give exactly the Young modulus (E_e) and deformation at point D (ε_D), therefore two these values are used the results of the coupon tests in ATTEL project [4] where the specimens extracted from the bolt shanks are tested.

Because the area of section of the specimens after point D is not measured during the coupon tests, the gradient of the curve from point D' to point E' (E_{ex}) and the deformation at point E' ($\varepsilon_{E'}$) are used the one in the literature [5].

The following values are calculated:

$\varepsilon_A = \sigma_A / E_e$ $\sigma_{A'} = \sigma_A(1+\varepsilon_A)$; $\varepsilon_{A'} = \ln(1+\varepsilon_A)$; $\sigma_{B'} = \sigma_B(1+\varepsilon_B)$; $\varepsilon_{B'} = \ln(1+\varepsilon_B)$; $\varepsilon_{C'} = \ln(1+\varepsilon_C)$; $\sigma_{C'} = \sigma_C(1+\varepsilon_C)$;
$\varepsilon_{D'} = \ln(1+\varepsilon_D)$; $\sigma_{D'} = \sigma_D(1+\varepsilon_D)$; $\sigma_{E'} = \sigma_{D'} + E_{ex}(\varepsilon_{E'} - \varepsilon_{D'})$.

Tables 5.3.2 and 5.3.3 present in detail the mechanical characteristics of the material.

For the specimens under monotonic loading, the isotropic hardening material is used, while the kinematical hardening material is adopted for specimens under repeated loading.

Table 5.3.2: The key values of the nominal curve (mean values)

	Plate 15mm	Plate 20mm	Tube	M27 bolts	M20 bolts
E_e (N/mm2)	210000				
ε_A (%)	0,18	0,18	0,39	0,41	0,40
ε_B (%)	2	2	-	-	-
ε_C (%)	8	8	-	-	-
ε_D (%)	15	15	8	3	3
σ_A (N/mm2)	387	384	822	857	850
σ_B (N/mm2)	387	384	-	-	-
σ_C (N/mm2)	527	512	-	-	-
σ_D (N/mm2)	544	529	881	930	930

Table 5.3.3: The key values of the natural curve

	Plate 15mm	Plate 20mm	Tube	M27 bolts	M20 bolts
E_e (N/mm2)	210000				
E_{ex} (N/mm2)	636			212	
$\varepsilon_{A'}$ (%)	0,18	0,18	0,39	0,4	0,4
$\varepsilon_{B'}$ (%)	1,98	1,98	-	-	-
$\varepsilon_{C'}$ (%)	7,7	7,7	-	-	-
$\varepsilon_{D'}$ (%)	13,98	13,98	7,7	3,0	3,0
$\varepsilon_{E'}$ (%)	100			90	
$\sigma_{A'}$ (N/mm2)	388	385	824	853	853
$\sigma_{B'}$ (N/mm2)	395	391	-	-	-
$\sigma_{C'}$ (N/mm2)	569	553	-	-	-
$\sigma_{D'}$ (N/mm2)	626	608	951	958	958
$\sigma_{E'}$ (N/mm2)	1153	1140	1536	1108	1108

D.5.3.4 Loading procedures

In order to take into account the preload state of the bolts, the loading procedure show on Fig.5.3.6 is used for the monotonic and the repeated loading. According to Eurocode-3, part 1.8, the pre-stress in the value of 509 N/mm2 is calculated with 8.8 bolt class.

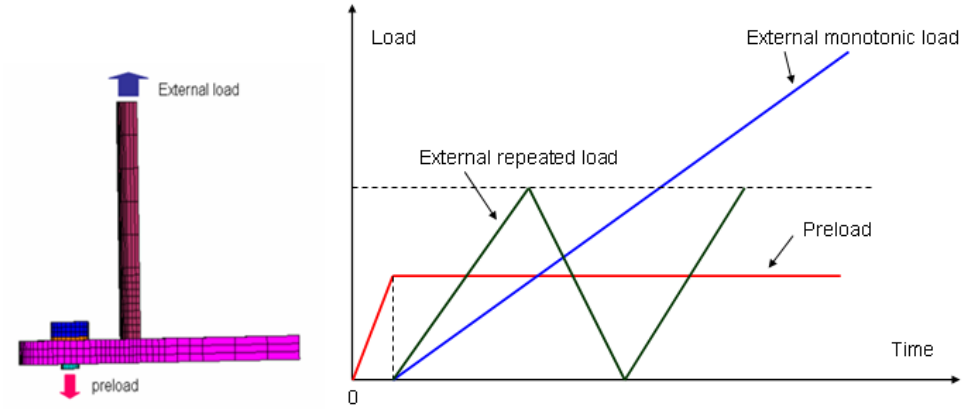

Fig.5.3.6. Loading procedure

D.5.3.5 Structural hot-spot stress determination

Normally, the stress distribution through plate thickness at the weld toes is nonlinear due to the notch effect. This distribution of stress may be decomposed into three parts: membrane stress, bending stress and the nonlinear peak. The structural hot spot stress composes the membrane and the bending stress, the nonlinear peak is not included (Fig.5.3.7).

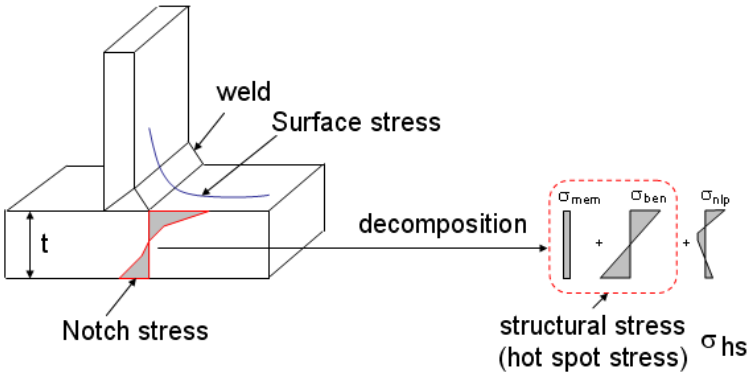

Fig.5.3.7. Hot spot stress definition

D.5.3.6 Methods for determining the hot spot stress

We use three methods that are usually adopted in the literature to determinate the hot spot stress in the plate at the weld toes, they are: (1) Linear surface extrapolation method (LSE) [6]; (2) Through thickness at the weld toe method (TTWT) [7]; (3) Structural stress from the distance method (Dong method) [8]. Main ideas of the methods are summarized on Figs. 5.3.8-5.3.10, the more detail about these methods may be found in the corresponding references. The comparisons of the methods are also presented in many works [9-12]. Let us note that: only τ_{xz} (Fig. 5.3.11) is taken into account in Dong proposal [7], but the influence of τ_{yx} and τ_{yz} is also important in some cases [9].

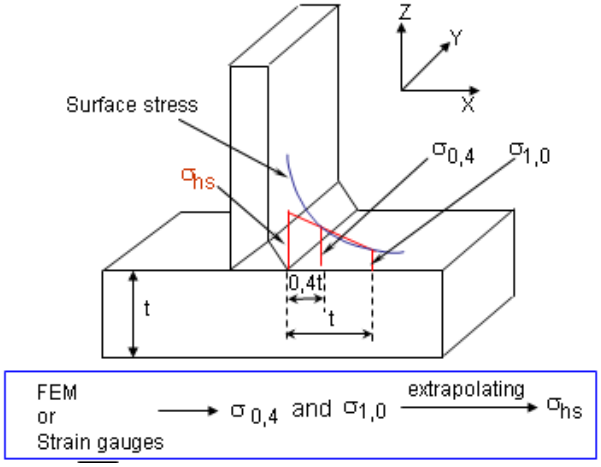

Fig.5.3.8. Linear surface extrapolation method

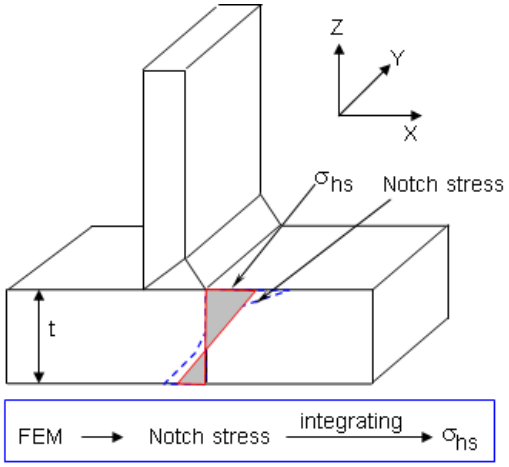

Fig.5.3.9. Through thickness at the weld toe method

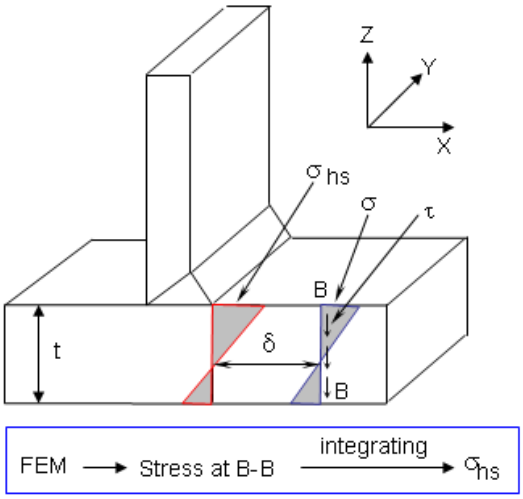

Fig.5.3.10. Structural stress from the distance method (Dong method)

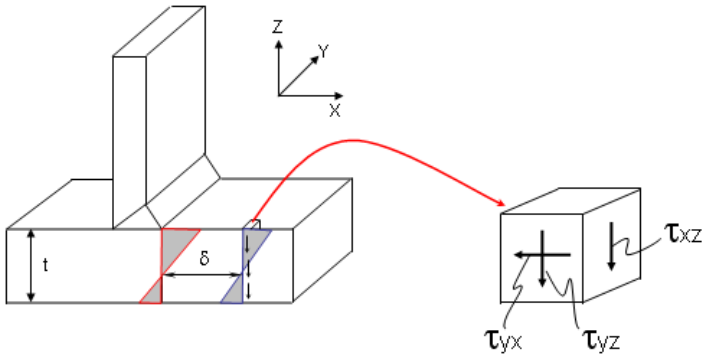

Fig.5.3.11. Shear stress components influence to the hot spot stress given by Dong method

D.5.3.7 Discussion

The hot spot stress in the flange at the weld toe was calculated by using the aforementioned methods. By means of the Dong's method, the variations of the distance δ and of the shear stress components are considered. The comparison of the hot spot stress given by the methods is shown on Fig.5.3.12. It points out that when the value of δ is small and all components of shear stress are considered, the hot spot stress coming from the Dong's method is in agreement with the one of the through thickness at weld toe method. On the other hand, it seems that the linear surface extrapolation method is not recommended in the present case; it may be due to the complicated distribution of the stress in the hot zone as the show on Fig.5.3.13. In conclusion, the hot spot stress provided by through thickness method should be used in the calculation of the present modelling.

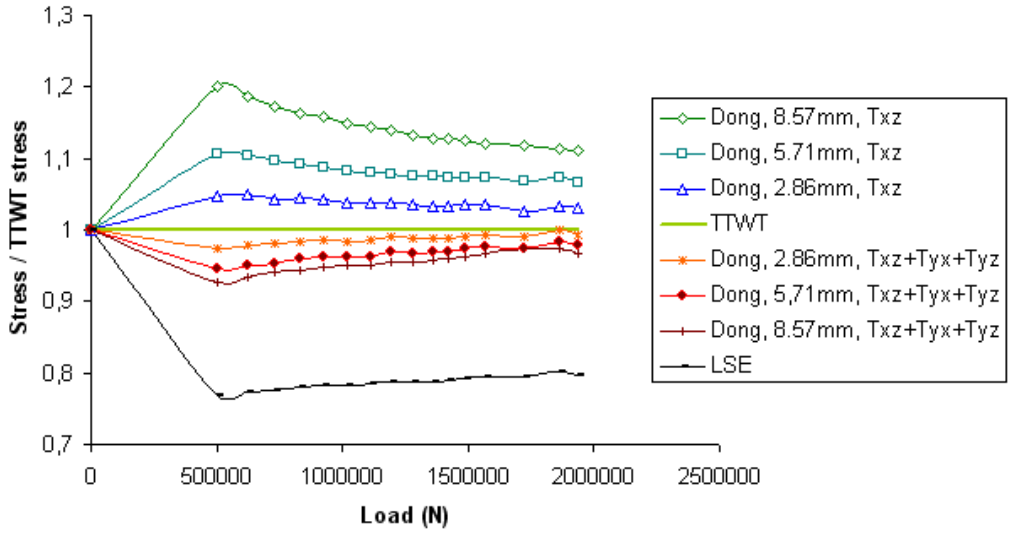

Fig.5.3.12. Comparison of the methods

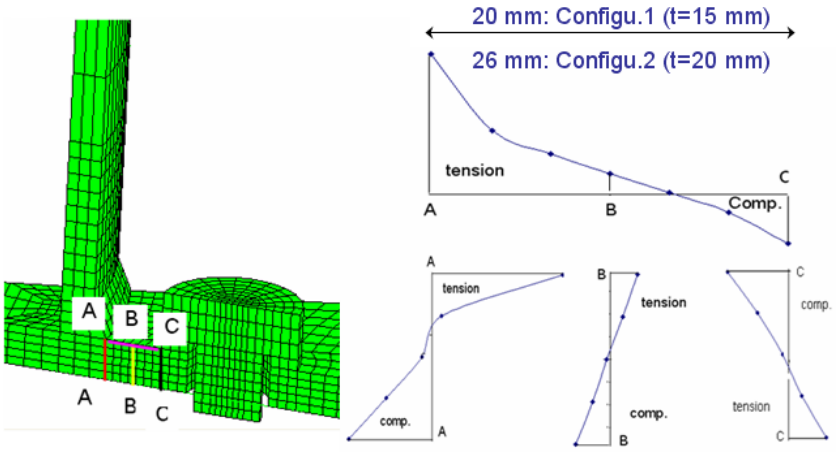

Fig.5.3.13. Stress distribution in the hot zone

D.5.3.8 Results: comparison with the experimental results

- *Comparison on the displacement*: The displacements given the numerical simulation are compared with the one of the tests under the monotonic and the repeated loading (Tests T1, T2, T5b, T6, see D4.4 [1]). Figs.5.3.14-5.3.18 show the comparison procedure, good agreement is observed.

- *Comparison on the deformation (failure mode for the specimens under the monotonic and repeated loading)*: The deformation of the specimens under monotonic loading (Test T1 and T2) is comparison as the show on Figs.5.3.19 and 5.3.20. We can say the mode 2 occurs in the configuration 1 and the mode 3 occurs in the configuration 2.

- *Comparison on the stress range (failure mode for the specimens under high cycle fatigue loading)*: As the description in D4.4 [1], the stress measurement was carried out carefully in almost tests. The stress range given in some tests are compared with the numerical analysis as the present on Figs.5.3.21-5.3.24, good agreement is observed. The stress range in the tube at the weld toe is most important leading to the fissures occur at this zone.

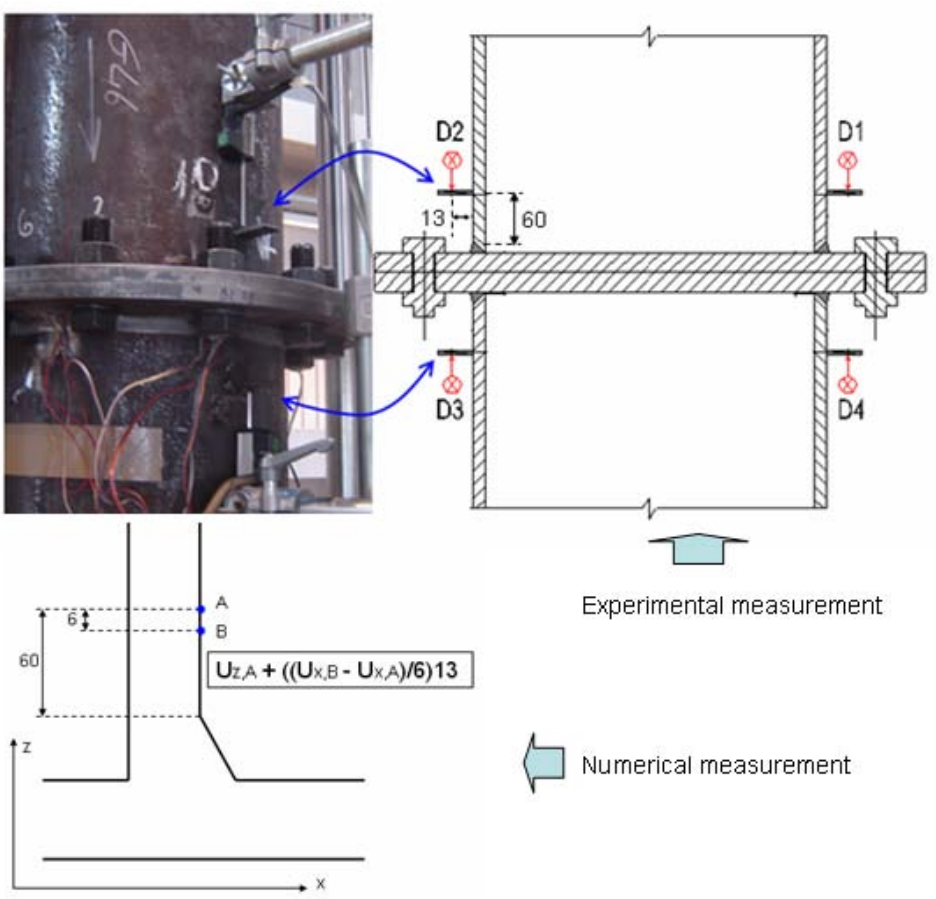

Fig.5.3.14. Measurement of displacement

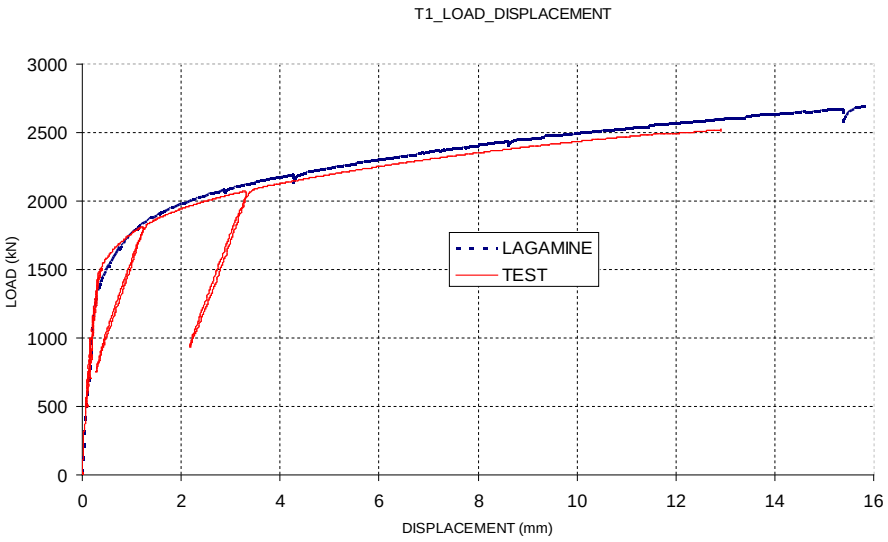

Fig.5.3.15. Load-displacement curve of the joint configuration 1

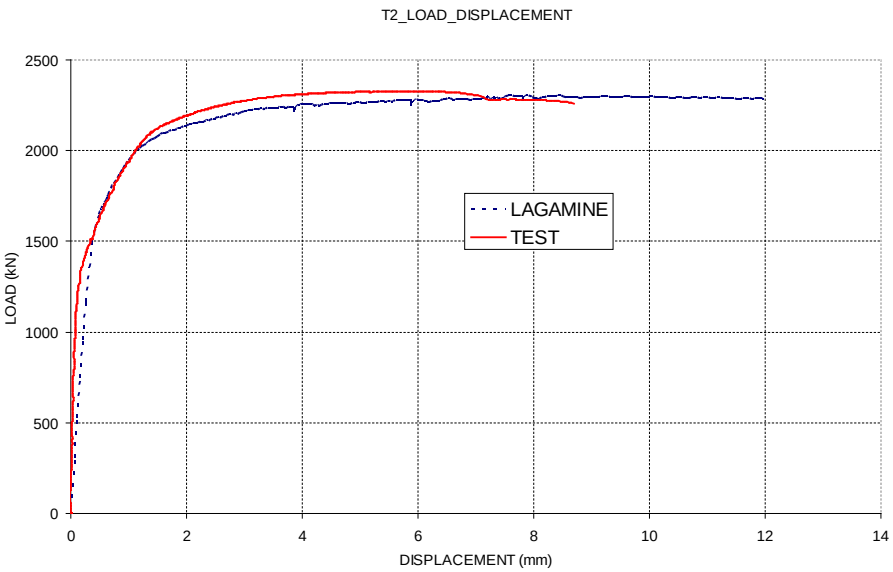

Fig.5.3.16. Load-displacement curve of the joint configuration 2

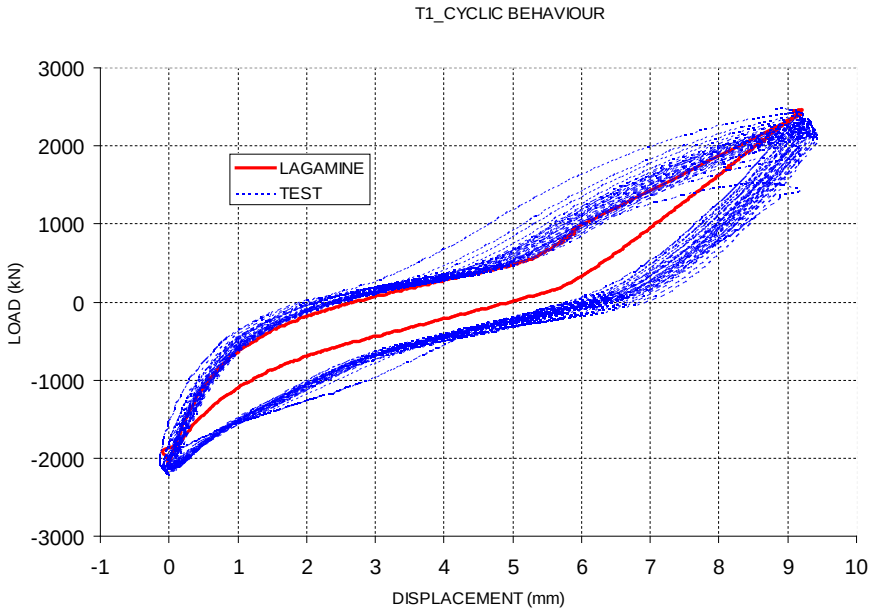

Fig.5.3.17. Comparison of cyclic behaviour (configuration 1)

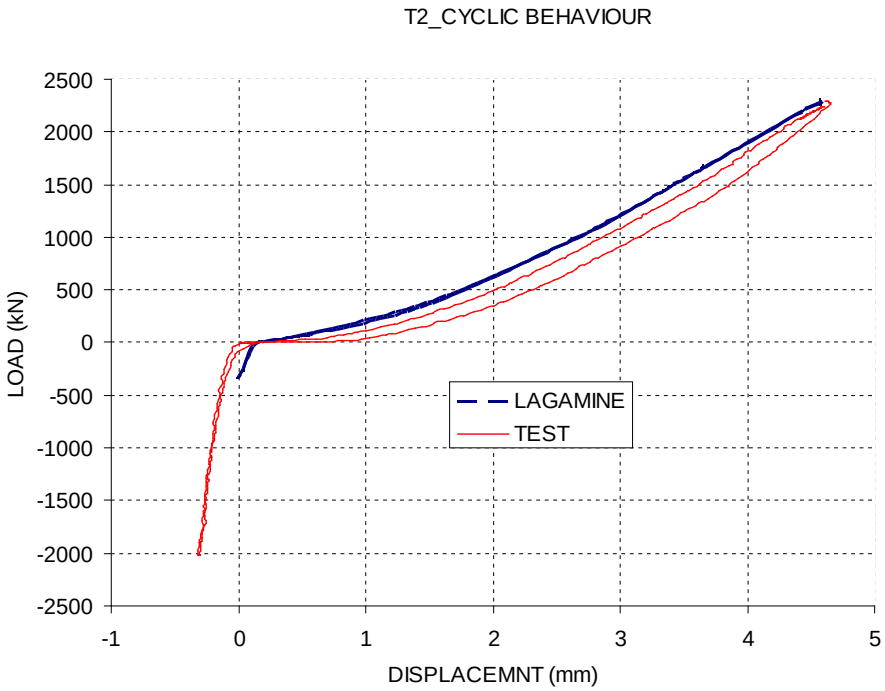

Fig.5.3.18. Comparison of cyclic behaviour (configuration 2)

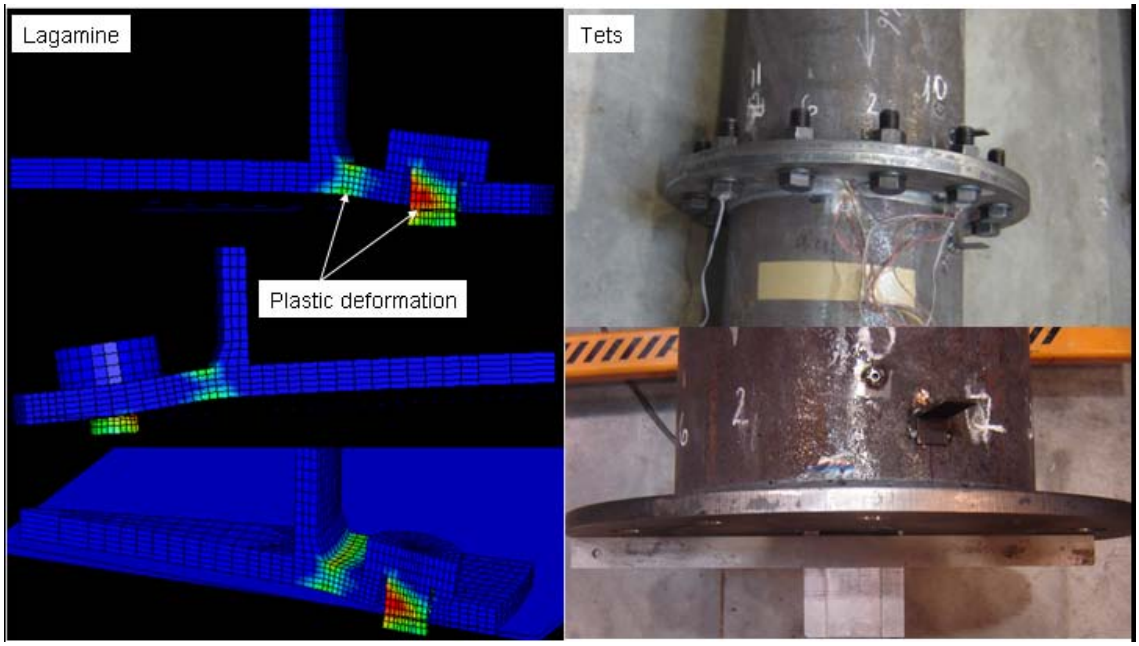

Fig.5.3.19. Deformation comparison (configuration 1)

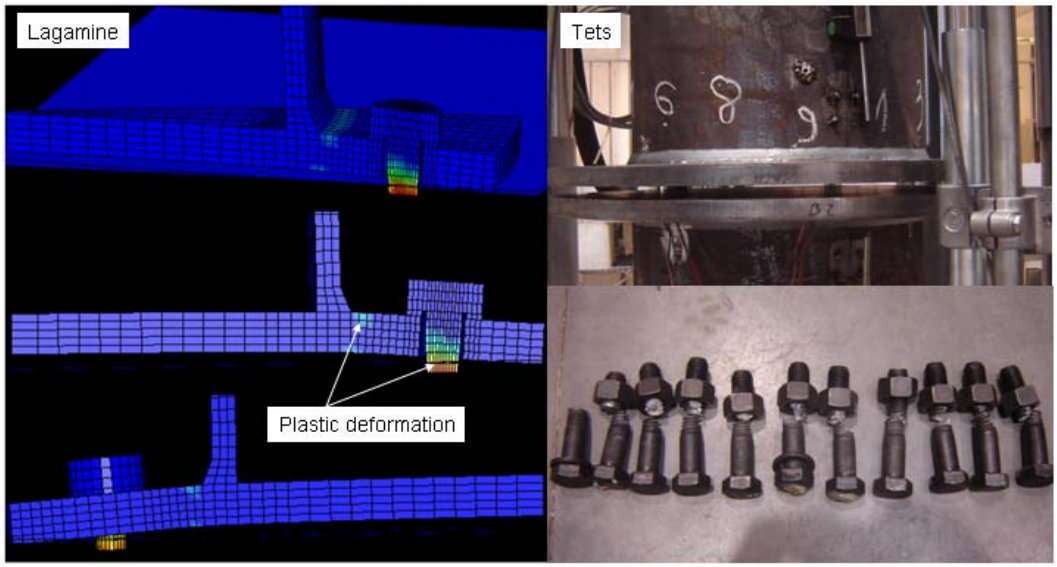

Fig.5.3.20. Deformation comparison (configuration 2)

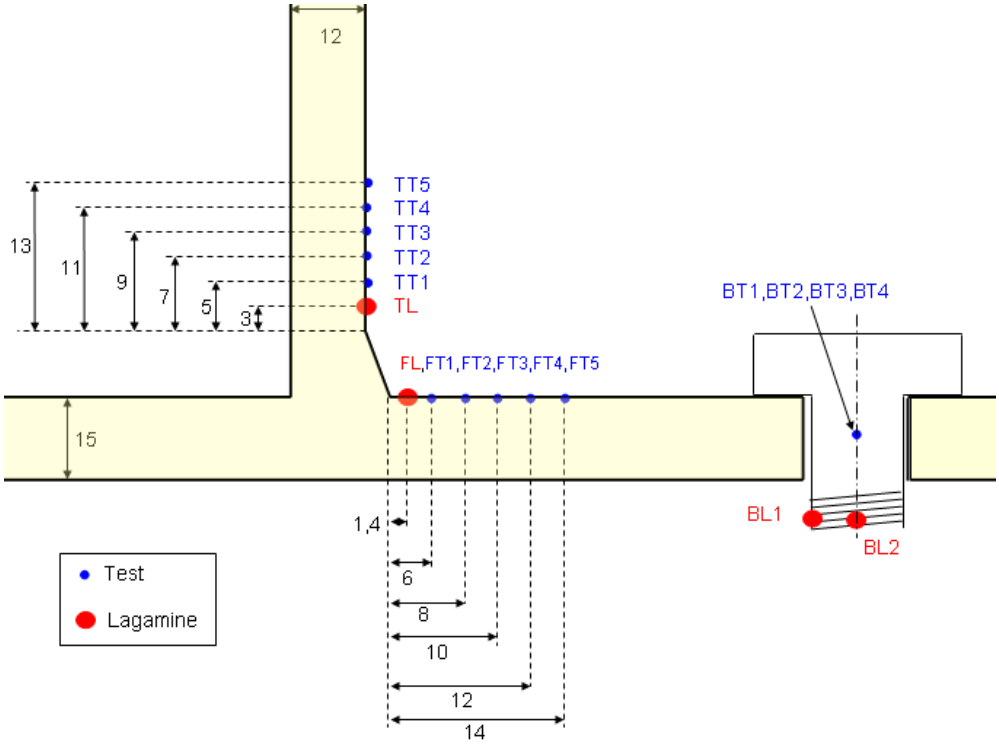

Fig.5.3.21. Measurement of stress

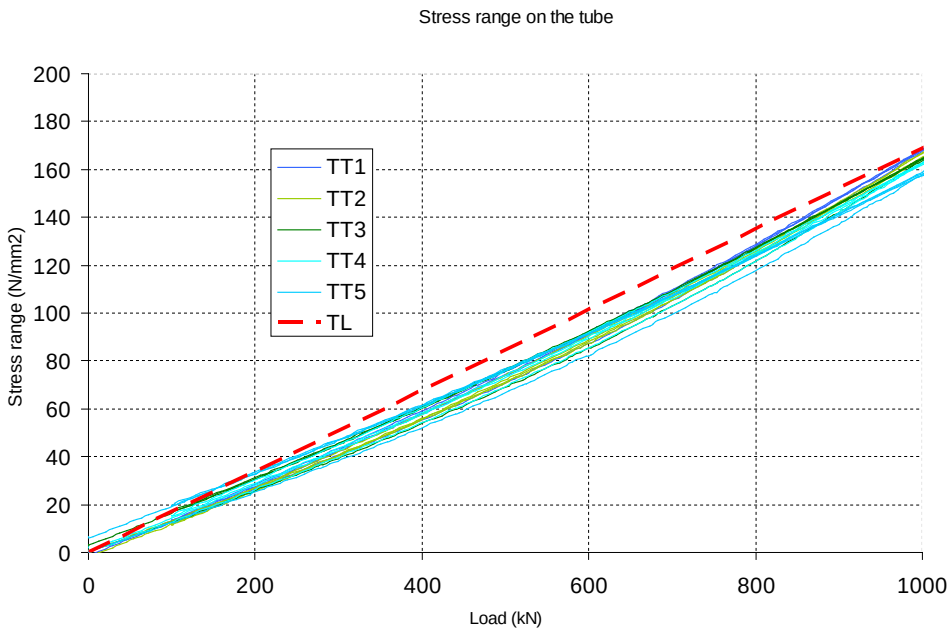

Fig.5.3.22. Comparison of the stress range on the tube at the weld toe (configuration 1)

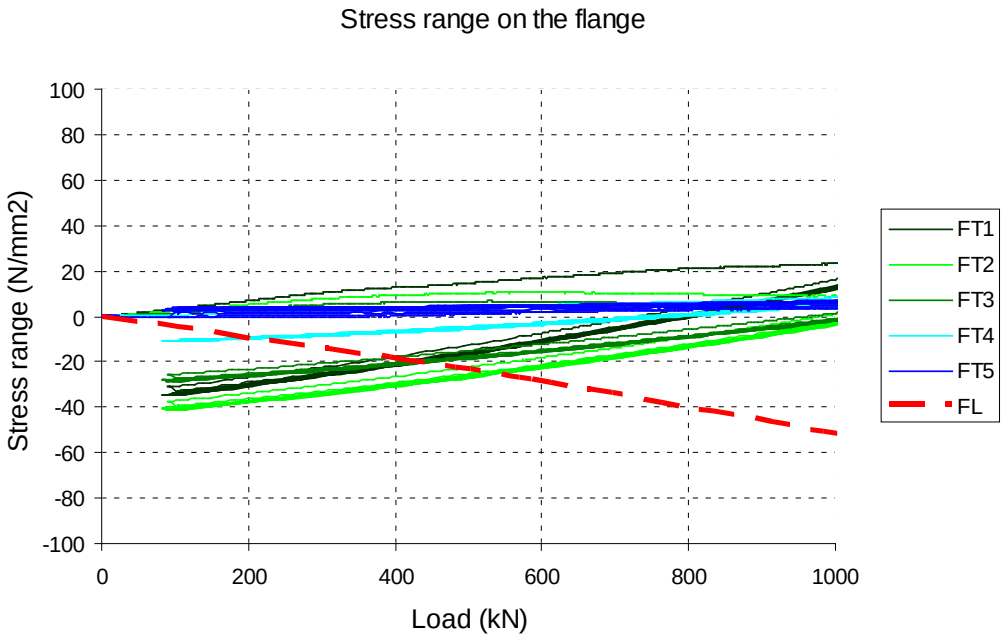

Fig.5.3.23. Comparison of the stress range on the flange at the weld toe (configuration 1)

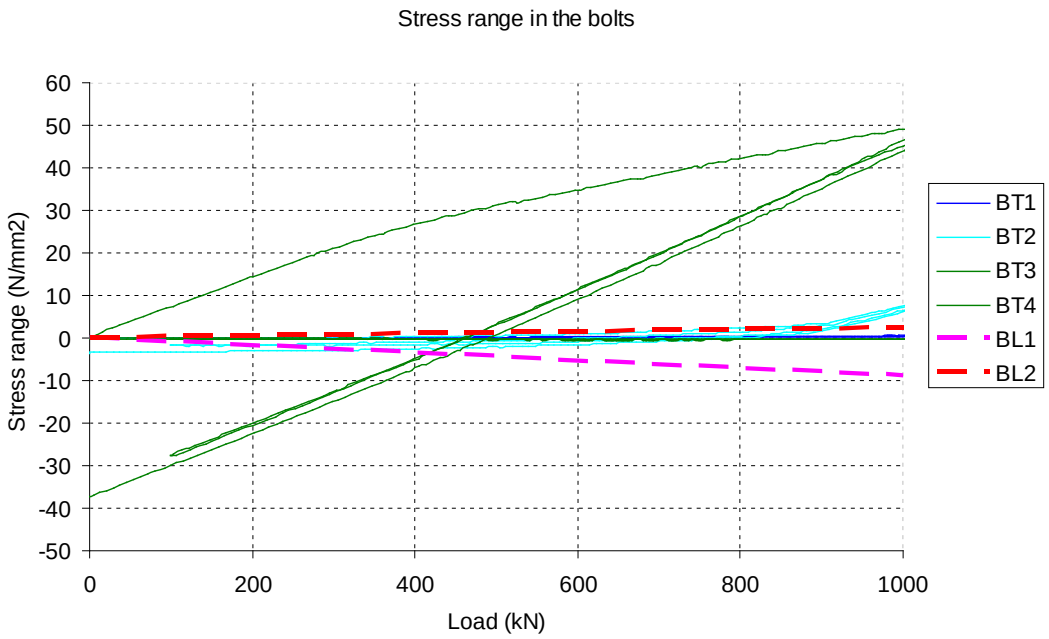

Fig.5.3.24. Comparison of the stress range in the bolts (configuration 1)

D.5.3.9 Concluding remarks

The adequate models were applied in the simulation: 3D solid element with large deformation and elastic-plastic nonlinear material are used, contact problem was considered, initial geometric imperfection of the flange was included, etc. The good agreement with the experimental results, in the both kinematical and static aspects, confirmed the correctness of the model. Thus, we can generate a reliable FE model for the parametric study of joints.

D.5.3.10 References

[1]. HITUBES project, Deliverable D 4.4- Annex A3 of the Six-monthly report, September 2011.

[2]. User's manual for LAGAMINE, University of Liege, 2010.

[3]. Agreskov. H. High strength bolted connections subject to prying. J. Struc Div 1976.

[4]. ATTEL project, Deliverable D 4, 2011.

[5]. Couchaux Mael. Comportement des assemblages par brides circulaires bouonnes. PhD thesis, INSA of RENNES, France.

[6] A. Hobbacher. Recommandations for fatigue design of welded joints and components. IIW 2005.

[7] D. Radaj. Design and analysis of fatigue resistant welded structures. Abington Publishing 1990.

[8] P. Dong. A structural stress definition and numerical implementation for fatigue analysis of weld joints. International Journal of Fatigue 23 (2001) 865-876.

[9] I. Poutiainen et al. Finite element methods for structural hot spot stress determination – a comparison of procedures. International Journal of Fatigue 26 (2004)1147-1157.

[10] M.H. Kim et al. A comparative study for the fatigue assessment of a ship structure by use of hot spot stress and structural stress approaches. Ocean Engineering 36 (2009) 1067 – 1072.

[11] O. Doerk et al. Comparison of different calculation methods for structural stresses at welded joints. International Journal of Fatigue 25 (2003) 359-369.

[12] W. Fricke, A. Kahl. Comparison of different structural stress approaches for fatigue assessement of welded ship structures. Marine Structures 18 (2005) 437 – 488.